

Evaluating the effects of high-throughput structural neuroimaging predictors on whole-brain functional connectome outcomes via network-based vector-on-matrix regression

Tong Lu¹, Yuan Zhang², Vince Lyzinski¹, Chuan Bi³, Peter Kochunov⁴, Elliot Hong⁴, Shuo Chen^{3,5}

¹Department of Mathematics, University of Maryland, College Park

² Department of Statistics, The Ohio State University

³Maryland Psychiatric Research Center, School of Medicine, University of Maryland

⁴Department of Psychiatry and Behavioral Science, University of Texas Health Science Center

⁵Division of Biostatistics and Bioinformatics, School of Medicine, University of Maryland

*shuochen@som.umaryland.edu

Abstract

The joint analysis of multimodal neuroimaging data is critical in the field of brain research because it reveals complex interactive relationships between neurobiological structures and functions. In this study, we focus on investigating the effects of structural imaging (SI) features, including white matter micro-structure integrity (WMMI) and cortical thickness, on the whole brain functional connectome (FC) network. To achieve this goal, we propose a network-based vector-on-matrix regression model to characterize the FC-SI association patterns. We have developed a novel multi-level dense bipartite and clique subgraph extraction method to identify which subsets of spatially specific SI features intensively influence organized FC sub-networks. The proposed method can simultaneously identify highly correlated structural-connectomic association patterns and suppress false positive findings while handling millions of potential interactions. We apply our method to a multimodal neuroimaging dataset of 4,242 participants from the UK Biobank to evaluate the effects of whole-brain WMMI and cortical thickness on the resting-state FC. The results reveal that the WMMI on corticospinal tracts and inferior cerebellar peduncle significantly affect functional connections of sensorimotor, salience, and executive sub-networks with an average correlation of 0.81 ($p < 0.001$).

Keywords: multi-level graph, brain connectome, structural measures, functional connectivity, dense clique

1 Introduction

Neuroimaging data play a fundamental role in deciphering the operations of the human brain, the most complex organ. These data come in various modalities, including magnetic resonance imaging

(MRI), diffusion tensor imaging (DTI), and functional MRI (fMRI). Each modality reveals distinct aspects of the brain’s structure and functionality. For example, MRI provides high-resolution images of the brain’s structure, offering valuable physical information such as size, shape, and cortical thickness. DTI assesses the integrity of white matter microstructures by calculating fractional anisotropy. The fMRI data capture dynamic blood flow changes in different brain regions to measure localized neural activity and functional connections.

In statistical analysis, neuroimaging data are commonly represented in two forms: vectors (e.g., a list of region-wise cortical thickness measures) and association matrices (e.g., functional connectivity strengths stored in a weighted adjacency matrix) (Bullmore and Sporns, 2009; Wig et al., 2014; Fornito et al., 2016; Wang et al., 2023). Instead of studying brain structural imaging (SI) and functional connectivity (FC) data separately, exploring their intricate interplay could significantly deepen our understanding of the brain, including its development and aging (Smith et al., 2004; Drevets et al., 2008; Bowman et al., 2012; Kemmer et al., 2018). For example, brain regions connected by white matter tracts with higher fractional anisotropy are more likely to demonstrate strong FCs, which, in turn, can influence cognitive processes such as attention, memory, and decision-making.

There exists little work on the joint analysis of multi-modal neuroimaging data despite its clear importance, possibly due to the challenge presented by ultra-high dimensionality and intertwined data structures. In conventional brain connectome studies, researchers frequently collect 10^5 FC measures across hundreds of brain regions and up to 10^4 SI measures, resulting in billions (10^9) of FC-SI pairs. This not only creates significant computational demands but also poses challenges for multiple-testing correction. Traditional correction methods like the false discovery rate (FDR) and family-wise error rate (FWER) often yield almost no supra-threshold FC-SI pairs, as demonstrated by extensive simulation studies. Moreover, FC and SI display data structures indicative of certain connectomic network space and spatial dependence, respectively. A joint FC-SI analysis needs to incorporate these intertwined data structures into comprehensive statistical modeling, thus producing biologically plausible and interpretable results. Specifically, our goal in this work is to identify an array of SI variables that intrinsically influences a group of FCs within a brain connectome sub-network, rather than those randomly distributed across the whole-brain connectome, referred to as a systematic pattern of associations. These challenges underscore the necessity of developing a joint analysis method to address the complexity of multi-modal neuroimaging data.

Recently, advanced statistical methods have been developed to jointly model two sets of neuroimaging features by leveraging techniques including regularization, low rank, and projection models (Wang et al., 2011; Li et al., 2012; Zhu et al., 2014; Kong et al., 2019). Many of these methods have been successfully applied to multi-modal imaging data analysis and yielded interesting findings (Hayden et al., 2006; Ball et al., 2017; Wehrle et al., 2020; Zhang et al., 2022). These statistical methods can be broadly classified into two categories. The first category uses regularization-based methods (Zhou and Li, 2014; Zhu et al., 2017; Wang et al., 2020), where a major limitation of these methods is that the sparsely selected associations fail to take into account the systematic network-level impacts of SIs on FC networks. The second category employs dimensional reduction strategies, such as principal component analysis (PCA) (Hotelling, 1933; Jolliffe and Cadima, 2016; Chachlakis et al., 2019), which first projects both FCs and SIs into a handful of top principal components and then performs regression analysis on these selected components. However, as an unsupervised dimension reduction technique, PCA-based analysis often extracts fewer associated principal components of outcomes and predictors, thereby missing the truly associated FC-SI

pairs. Sparse canonical correlation analysis (sCCA) methods can be considered as an integration of these two categories and have been widely used in neuroimaging studies (Witten et al., 2009; Lin et al., 2013; Urtio et al., 2019). Yet, sCCA methods usually focus on vector-to-vector association analysis, which may also overlook the systematic vector-to-network association patterns that are of particular interest in this work (i.e., the associations between the SI vector and FC sub-connectome represented as a matrix). To bridge the methodological gap in modeling vector-to-matrix associations and incorporating latent network structures, we propose a new **multi-level network association method (MOAT)** to systematically investigate the FC-SI association patterns.

Figure 1 presents an overview of the MOAT method, which is constructed based on a multi-level graph for structural-functional neuroimaging data. The first level is a bipartite graph that depicts the association patterns between the SI vector as predictors and vectorized FC outcomes, adjusted for other confounding covariates (Figure 1(a)). Meanwhile, the second level is a complete unipartite graph that reconstructs the vectorized FCs back to a whole-brain connectome network. This multi-level structure enables the identification of subsets of SIs that systematically impact FC sub-networks. We have further developed computationally efficient algorithms to extract the multi-level sub-networks from the full graphs and have proposed a tailored network-based inference frame to individually test each sub-network with multiple corrections based on permutation tests. Our method is also compatible with the existing methods aforementioned (e.g., PCA, CCA). For example, applying CCA to FCs and SIs in an extracted multi-level sub-network provides an estimate of association in the context of multiple regressions.

The contributions of this article are three-fold. First, we introduce MOAT, a novel method that can handle matrix-variate outcomes and vector-variate predictors. Compared to the existing models for multivariate outcomes and multivariate predictors (Zhuang et al., 2017; Wu et al., 2021; Mihalik et al., 2022; Lu et al., 2023), MOAT can further account for the network structure within the matrix outcomes and between the outcome-predictor association patterns. MOAT naturally prohibits most false positive associations because these associations are more likely distributed sparsely rather than gathered in organized sub-networks. Secondly, we develop new algorithms to extract those multi-level sub-networks. The computational load is low because we developed a tailored greedy peeling algorithm with multilinear complexity, making our approach compatible with the commonly used permutation tests that are often computationally intensive. Lastly, we proposed a novel network-level inference framework, where we utilize novel test statistics derived based on the multi-level dense subgraph properties in terms of size and density. This inference framework leads to a simultaneous enhancement of both sensitivity and specificity by leveraging graph combinatorial theories.

The rest of this paper is organized as follows. In Section 2, we formally define the multi-level network structure and present how MOAT works in network extraction with the network-based inference method. In Section 3, we perform extensive simulation analyses for method validation and comparison. In Section 4, we apply MOAT to a real structure-function neuroimaging dataset from the UK Biobank with 4,242 participants to systematically investigate the FC-SI associations. We conclude with discussions in Section 5.

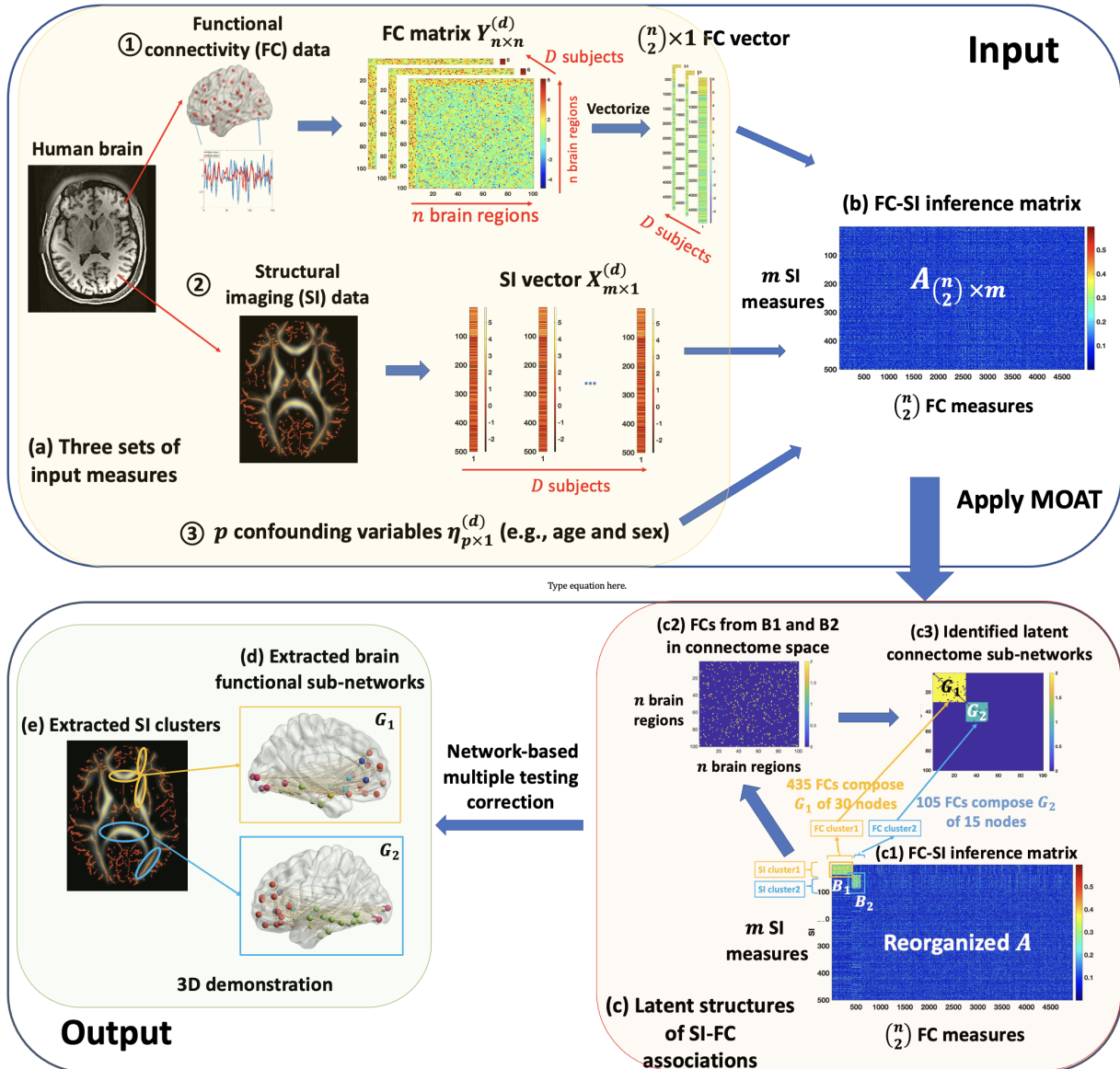


Figure 1: The detection pipeline of systematic FC-SI association patterns by MOAT. (a) shows three sets of input measures: FC data, SI data, and confounding variables. (b) shows a heatmap of an association matrix A , with each element quantifying the association between SI and FC measures (e.g., correlation, test statistics, $-\log(p)$ value). A hotter point indicates a stronger FC-SI association. (c) shows the systematic FC-SI association patterns identified by MOAT: the first level (c1) depicts the revealed association patterns between SIs and FCs, where strong associations are mostly concentrated in two dense sub-networks; (c2) shows the FCs in brain connectome space from the detected clusters B_1 and B_2 in (c1); (c3) shows the second level, which depicts the organized structure of a graph formed by the selected FC clusters in (c2). Next, our proposed network-based inference test is performed on each FC-SI sub-network identified by MOAT. (d) and (e) shows the 3D visualization of the significant FC-SI network-level associations that pass the inference test.

2 Our method

2.1 Data structure and problem set up

We collect structural-functional neuroimaging data from independent subjects, indexed as $\{1, \dots, D\}$. For each subject $d : 1 \leq d \leq D$, we observe three sets of measurements:

- (i) Independent variables: a vector of m SI measures $\mathbf{X}^{(d)} = (x_1^{(d)}, \dots, x_m^{(d)})^T$. This vector characterizes anatomical structures of the brain, such as white matter microstructure integrity measured by fractional anisotropy from DTI (Mori et al., 2008) and region-wise cortical thickness obtained from MRI (Tustison et al., 2014).
- (ii) Outcome variables: an adjacency matrix that stores pairwise FC measures $\mathbf{Y}_{n \times n}^{(d)}$ between n brain regions. Each element $y_{ij}^{(d)}$ of $\mathbf{Y}^{(d)}$ represents the strength of functional connection between brain regions i and j of subject d , calculated from functional imaging data such as resting state fMRI. Thanks to the Brainetcome Atlas (Fan et al., 2016), researchers can align the FC brain region partitions across different participants, thus conveniently, their \mathbf{Y} share a common node set. We model $\mathbf{Y}^{(d)}$ as the outcome variable due to the widely accepted view in neurology that brain structure determines neural functions (Buckner et al., 2008; Bai et al., 2009; Honey et al., 2010).
- (iii) Confounding variables: $\boldsymbol{\eta}^{(d)} = (\eta_1^{(d)}, \dots, \eta_p^{(d)})^T$. These variables include profiling information such as age, sex, genetics, and environment that may potentially affect brain functional connectome in complicated ways.

2.2 Multi-level graph representation

We explore the brain structural-functional relationship by considering the following regression model: for each subject $d \in [1, D]$,

$$g(y_{ij}^{(d)}) = \theta_{ij}^0 + \sum_{k=1}^m \beta_{(ij),k} x_k^{(d)} + \sum_{p=1}^P \alpha_{ij}^p \eta_p^{(d)}, \quad (1)$$

where $g(\cdot)$ is a link function, θ_{ij}^0 is the intercept, $\beta_{(ij),k}$ is the coefficient of the SI measure x_k , and α_{ij}^p is the coefficient of the nuisance covariate η_p (Zhang et al., 2023). The focal parameter of interest in the above regression model (1) is $\beta_{(ij),k}$, where a nonzero coefficient $\beta_{(ij),k} \neq 0$ signifies an association between an SI measure x_k and the functional connection y_{ij} between brain regions i and j . Consequently, learning the set $\{\beta_{(ij),k} \neq 0\}$ allows for the unveiling of brain-wide association patterns between SIs and FCs.

A multi-level graph model targeting $\{\beta_{(ij),k} \neq 0\}$ associations. To facilitate downstream analysis, we let a matrix $\boldsymbol{\beta} = \{\beta_{(ij),k}\}_{\forall ijk} \in \mathbb{R}^{\binom{n}{2} \times m}$ to denote all SI-FC pair-wise associations. (Zhang and Xia, 2018). We build the multi-level graph model based on the $\binom{n}{2} \times m$ matrix $\boldsymbol{\beta}$. Specifically, at the first level, we define a bipartite graph $B = (S, F; H)$ to represent the matrix $\boldsymbol{\beta}$, where $S = \{1, \dots, m\}$ (i.e., $|S| = m$) constitutes the node set of SI measures; $F = \{1, \dots, \binom{n}{2}\}$ (i.e., $|F| = \binom{n}{2}$) constitutes the node set of FC measures; and H denotes the edge set. Each element $h_{(ij),k} \in H$ signifies a non-zero association between FC and SI (i.e., $\beta_{(ij),k} \neq 0$). We demonstrate

the first level bipartite graph B in the left panel of Figure 2 . The second level of the multi-level graph model is a classic graph model reflecting the whole-brain connectome network, denoted as $G = (V; F)$, where V is the node set of brain regions with size $|V| = n$, while F is the edge set connecting brain regions with size $|F| \leq (n - 1)/2$. Noticeably, each node (i, j) in F can also be interpreted as an edge in the brain functional connectome network $G(V; F)$. Thus, F denotes both (i) the node set of the bipartite graph $B = (S, F; H)$ with $F = \{f_{(ij)}\}$, where $f_{(ij)}$ represents a node for the outcome Y_{ij} ; (ii) the edge set of $G(V; F)$ with $F = \{f_{i,j}\}$, where $f_{i,j} = 1$ indicates that brain areas i and j are connected.

Underlying structure of multi-level graph B and G

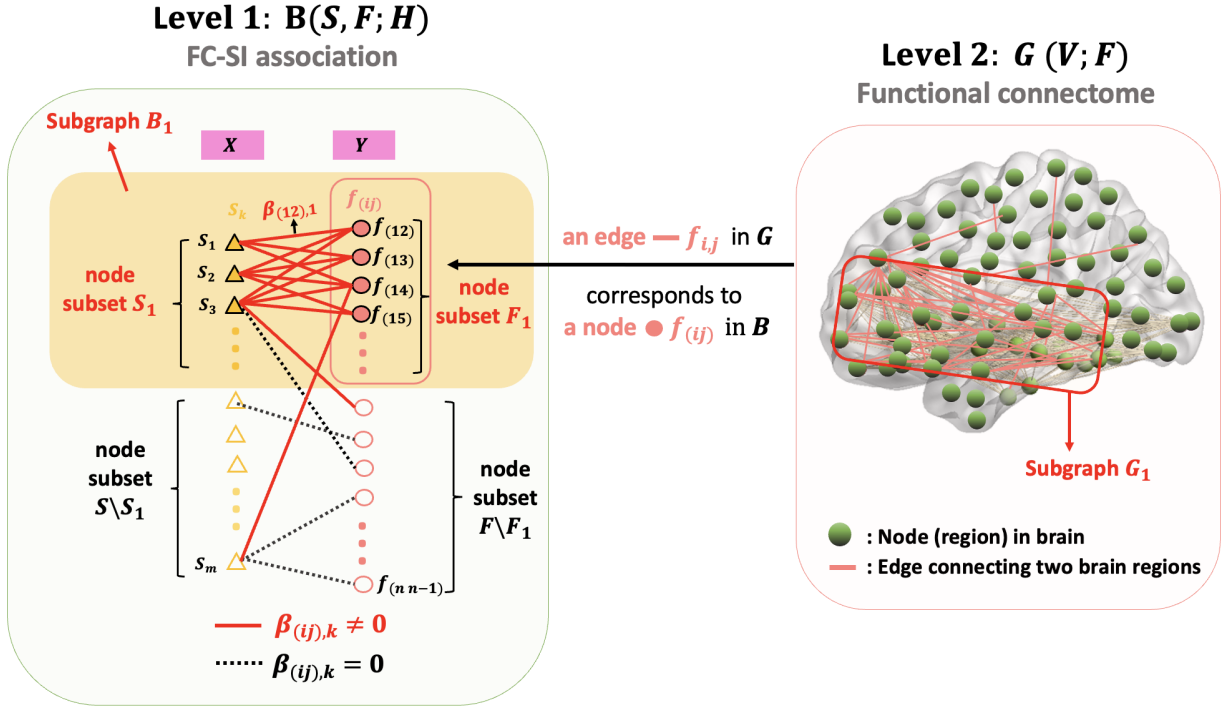


Figure 2: A toy example of a multi-level graph denoted as B and G , where there exists one sub-network $B_1 \in B$ exhibiting a significant association between FC and SI. In Level 1, $B = (S, F; H)$ is an input bipartite graph consisting of two node sets S and F , representing the SI and FC measures respectively. The edge set H is binary and determined by the regression coefficient $\beta = \{\beta_{(ij),k}\}$ which infers the association between y_{ij} (FC strength between brain regions i and j) and x_k (k -th SI measure). In this toy example, there exists a sub-network $B_1 = (S_1, F_1; H_1) \subset B$ which contains SI-related edges $\{h_{(ij),k} | i, j, k \in B_1\}$ with a much higher density than the rest $\{h_{(ij),k} | i, j, k \notin B_1\}$. Given that the node set F represents the whole-brain functional connectome, each node $f_{(ij)} \in F$ comes from an edge in a brain connectome graph $G = \{V; F\}$ (Level 2 graph), where V is the node set of brain regions, and F is the edge set of interregional connections. $\{f_{(ij)}\} \in B_1$ are not isolated in the brain connectome; instead, they constitute an organized sub-graph $G_1 \in G$.

In light of the highly organized brain structures and functions, it is neurobiologically sensible to model $\{\beta_{(ij),k} \neq 0\}$ in organized association patterns (Craddock et al., 2013; Bahrami et al., 2019). Specifically, we consider that a subset of brain structural predictors jointly influences connectome outcome variables within a functional subnetwork, which characterizes a plausible brain structure-

function interaction (Zalesky et al., 2010; Cao et al., 2014). Built upon this latent relationship pattern, we specify that $\{\beta_{(ij),k} \neq 0\}$ predominantly concentrates within specific subgraphs denoted as $\{B_c\}$ where $c = 1, \dots, C$ and $B_c \subset B$. For simplicity, we are going to illustrate the case where $c = 1$ below.

We specify $B_1(S_1, F_1)$ as a doubly-dense multi-level subgraph (see dense graph studied in Tong MOAT, Craddock et al. (2013); Wu et al. (2021)). At the first level, a subset of SI predictors of $\{X_k, k \in S_1\}$ condensely affect $\{Y_{ij}, ij \in F_1\}$:

$$\Pr(\beta_{(ij),k} \neq 0 \mid (ij) \in F_1, k \in S_1) \gg \Pr(\beta_{(ij),k} \neq 0 \mid (ij) \notin F_1 \text{ or } k \notin S_1). \quad (2)$$

At the second level, a connectomic subnetwork $G_1 = (V_1; F_1)$ is an edge-induced sub-clique, where the edge subset of interest is $\{(i, j) : (ij) \in F_1\}$. G_1 is also dense reflecting that SIs of S_1 are associated with connectomic edges in a network rather than sparsely and randomly distributed in the whole-brain connectome (ref Tong 2023). In Figure 2, we demonstrate a doubly-dense multi-level subgraph B_1 with red-bold edges. Provided with $\{B_c\}$, we can express the overall multi-level graph as (3) and (4) as follows:

$$\text{Level 1 (bipartite) network: } B = \cup_{c=1}^C B_c \cup B_0, \quad B_c = (S_c, F_c; H_c); \quad (3)$$

$$\text{Level 2 (unipartite) network: } G = \cup_{c=1}^C G_c \cup G_0, \quad G_c = (V_c; F_c), \quad (4)$$

where B_c and G_c are dense subgraphs in B and G respectively, and B_0 and G_0 are the remaining graphs. Each node set F_c in B_c corresponds to a subset of edges in the functional connectome G , which induces one or multiple cliques in G . For simplicity, we use G_c to denote the clique(s) for the corresponding B_c . If B is a random graph, then $B = B_0$ and for all $c = 1, \dots, C$, $B_c = \emptyset$. Similarly, if G is a random graph, then $G_c = \emptyset$. Otherwise, G_c represents a connectome sub-network. In Figure 2, we demonstrate a graphical example of the multi-level structure of B_c and G_c when $c = 1$. In summary, our multi-level network model assigns a small proportion of $\{\beta_{(ij),k} \neq 0\}$ to structured subnetworks reflecting systematic FC-SI association patterns. The patterns may not be captured by neither shrinkage regression models nor clustering/biclustering methods.

2.3 Multi-level subnetwork estimation

In practice, neither $\{\beta_{(ij),k} \neq 0\}$ nor $\{B_c\}$ is known and it is challenging to simultaneously handle billions of FC-SI associations and estimate $\{B_c\}$ ($\{\beta_{(ij),k} \neq 0\}$) in one big model such as (1) (Woo et al., 2014; Mbatchou et al., 2021; Marek et al., 2022). To alleviate the computation burden, we take a divide-and-conquer approach and run one regression for each k , recognizing that both θ and α may also be different for each k . This strategy is commonly used in large-scale imaging and genetics data analysis (Zalesky et al., 2010; Schaid et al., 2018; Chen et al., 2023).

Next, we extract the desired dense subgraphs $\{B_c\}$ based on $\mathbf{X}^{(d)}, \mathbf{Y}^{(d)}, \boldsymbol{\eta}^{(d)}$. Since $\{\beta_{(ij),k} \neq 0\}$ are unknown, we compute an inference measure $a_{(ij),k}$ as a surrogate to $\beta_{(ij),k}$: each $a_{(ij),k}$ is produced by the statistical inference of a regression model for x_k and y_{ij} . For example, $a_{(ij),k}$ can be the $-\log(p)$ for $\beta_{(ij),k}$, where $-\log(p)$ is a widely used metric in high-dimensional data analysis, such as Genome-wide association studies (GWAS) and neuroimaging analysis (Lasky-Su et al., 2008; Tang et al., 2016; Sun et al., 2022). Now we propose the following criterion for selecting (S_1, F_1) :

$$\arg \max_{S_c \subseteq S, F_c \subseteq F, V_c \subseteq V} \sum_{c=1}^C \frac{\sum_{k \in S_c, (ij) \in F_c} a_{(ij),k}}{\left(|S_c| \binom{|V_c|}{2}\right)^{\lambda_1/2}} + \frac{\sum_{i,j \in V_c, i < j} f_{ij}}{|V_c|^{\lambda_2}}, \quad (5)$$

where λ_1, λ_2 tune the impacts of the densities of B_c and G_c , respectively. For example, when $\lambda_1 = 2$, the first term becomes the familiar quantity of subgraph density in network analysis. We typically search λ_1 within the range of $(1, 2)$. Empirically, setting $\lambda_1 = 2$ usually forces B_c 's into singletons; while setting λ_1 below 1 often leads to sparse B_c 's. Likewise, we explore the parameter λ_2 within the same interval $(1, 2)$. Deviating from this range for λ_2 , either higher or lower, will yield results similar to those observed for λ_1 . Here, we follow the convention in neuroimaging analysis and select λ_1 and λ_2 using Kullback–Leibler (KL) divergence (Johnson and Sinanovic, 2001; Yohai, 2008; Zhao et al., 2023). Detailed selection procedures are provided in Appendix A.

Directly solving (5) requires combinatorial computation. Therefore, we propose a greedy peeling algorithm as a fast approximation. Our algorithm extends the greedy algorithm for single-level bipartite subgraphs extraction in Wu et al. (2021) and Chekuri et al. (2022). We present a condensed version as Algorithm 1 below, and relegate the detailed step-by-step algorithm to Appendix B. For each multi-level subgraph B_c and G_c , Algorithm 1 first initializes node sets S_c and F_c with the nodes S and F from the original full graphs, respectively. It then iteratively removes nodes with the smallest degree (say, $\tau \in S_c$ and $\phi \in F_c$) from either S or F (see Line 5 of the algorithm). At the end of each iteration q , the updated node set $F_c^{(q)}$ is used to construct the “level 2” subgraph $G_c^{(q)}(V_c; F_c)$, and the corresponding output value of objective function (5) is recorded. This process of node removal and the construction of “level 2” graph continues iteratively until all nodes have been excluded from S_c or F_c , with the termination determined by whichever node subset is exhausted first. Ultimately, the algorithm returns the dense subgraph B_c that maximizes (5) among all $\{B_c^{(q)}\}$ (see Line 14 of the algorithm).

The computational complexity of Algorithm 1 is $\mathcal{O}(\mathcal{C}|V|(|S| + |F|))$, where \mathcal{C} depends on the number of the grid search, $|V| = n$, $|S| = m$ and $|F| = \binom{n}{2}$ are the numbers of regions, SI measures, and FC measures, respectively. Additionally, Theorem 1 confirms the consistency of multi-level subgraph detection. In essence, the solution to the objective function (5) gives a consistent estimation of the true multi-level sub-network structure represented by B_c (the set of edge-induced sub-networks). As the sample size $D \rightarrow \infty$, the likelihood of an incorrect edge assignment for B_c approaches zero.

Theorem 1. (Consistency of subgraph detection). *let $\mathbf{U}^* \in \mathbb{R}^{|S| \times |F|}$ be a matrix storing the true edge membership in B , where each element $u_{(ij),k}^* = 1$ if $\beta_{(ij),k} \neq 0$, and $u_{(ij),k}^* = 0$ otherwise. Similarly, let $\hat{\mathbf{U}} \in \mathbb{R}^{|S| \times |F|}$ store the edge membership estimated by optimizing (5), where each element $\hat{u}_{(ij),k} = 1$ if $x_k \in \hat{S}_c$ and $y_{ij} \in \hat{F}_c$; $\hat{u}_{(ij),k} = 0$ otherwise. Then, for an arbitrarily small ϵ , when the sample size $D \rightarrow \infty$, we have*

$$\mathbb{P}(\|\mathbf{U}^* - \hat{\mathbf{U}}\|_F < \epsilon) \rightarrow 1,$$

where $\|\cdot\|_F$ denotes the frobenius norm.

The proof of Theorem 1 is provided in Appendix B.2.

Algorithm 1 Optimization of objective function (5) - Condensed pseudo code

Input: $B = (S, F; H)$, $G = (V, F)$, λ_1, λ_2
output: $\{B_c\}$

- 1: Define **function** $[B_c \text{ density}(B_c)] = \text{greedy_peeling_MOAT } [B \ G \ \lambda_1 \ \lambda_2]$:
- 2: Initialize "level 1" subgraph nodes $S_c^1 \leftarrow S, F_c^1 \leftarrow F$
- 3: **for** $q = 1, 2, \dots, m + \binom{n}{2} - 1$ **do**
- 4: Let $\tau \in S_c^{(q)}$ and $\phi \in F_c^{(q)}$ be the nodes with smallest degree
- 5: **If** $\sqrt{d}\tau \leq \frac{1}{\sqrt{d}}\phi$, **then** remove τ from $S_c^{(q)}$; **otherwise**, remove ϕ from $F_c^{(q)}$
- 6: Next, construct "level 2" subgraph $G_c(V_c; F_c)$, based on current F_c
- 7: Initialize "level 2" subgraph nodes $V_c^1 \leftarrow V$
- 8: **for** $p = 1, 2, \dots, n - 1$ **do**
- 9: remove node with smallest degree from $V_c^{(p)}$, store each $V_c^{(p)}$ and the corresponding $F_c^{(p)}$
- 10: **end for**
- 11: Output $G_c^{(q)}(V_c; F_c)$ that maximizes $\frac{\sum_{i,j \in V_c, i < j} f_{ij}}{|V_c|^{\lambda_2}}$ among $\{V_c^{(p)}, F_c^{(p)}\}_{p=1}^{n-1}$
- 12: Replace $F_c^{(q)}$ with $F_c^{(p)}$
- 13: **end for**
- 14: Output B_c that maximizes (5) among $\{B_c^{(q)}\}_{q=1}^{m + \binom{n}{2} - 1}$
- 15: **while** $\text{density}(B_c) > \text{density}(B)$ **do**
- 16: Fill median of $\{a_{(ij),k} | k \in S, (ij) \in F\}$ into $\{a_{(ij),k} | k \in S_c, (ij) \in F_c\}$, obtain updated B^* and G^*
- 17: $[B_c \text{ density}(B_c)] = \text{greedy_peeling_MOAT } [B^* \ G^* \ \lambda_1 \ \lambda_2]$
- 18: **end while**
- 19: Output all $\{B_c\}$

2.4 Reduced false positive findings by B_c

Compared to methods that *individually* select $\{\beta_{(ij),k}\}$ such as multiple testing approaches, our method selects nonzero β 's via *dense* FC-SI associated sub-network B_c , which can drastically reduce false positive findings. Let $\{\hat{\beta}_{(ij),k}\}$ denote the set of estimated association parameters from a sample; then $\{\hat{\beta}_{(ij),k} \neq 0 | \beta_{(ij),k} = 0\}$ indicate false positive findings. Following the common practice in neuroimaging and neurobiology (Margulis and Sagan, 2000), we assume that false positive associations are randomly distributed in the brain space. The conventional approach using individual inference on $\{\hat{\beta}_{(ij),k}\}$ may likely select many false positives $\hat{\beta}_{(ij),k} \neq 0 | \beta_{(ij),k} = 0$. In contrast, our method returns few false positives. The reason behind is demonstrated in the following lemma, which says false positives very rarely form dense subgraphs of moderate sizes.

Lemma 1. Assume that B_c is observed from a random multi-level binary graph with a bipartite graph $B(S, F; H)$ in Level 1 and a unipartite graph $G(V; F)$ in Level 2. Suppose that B_c is a multi-level subgraph that has: (1) Edge density in B_c with $\frac{\sum_{k \in S_c, (ij) \in F_c} I(\hat{\beta}_{(ij),k} \neq 0 | \beta_{(ij),k} = 0)}{|S_c| |F_c|} \geq \gamma_1 \in (p_1, 1)$, where $p_1 = \frac{\sum_{k \in S, (ij) \in F} I(\hat{\beta}_{(ij),k} \neq 0 | \beta_{(ij),k} = 0)}{|S| |F|}$ is the proportion of false positive associations in B ; (2) Edge density in G_c with $\frac{\sum_{i,j \in V_c, i < j} I(\hat{\beta}_{(ij),k} \neq 0 | \beta_{(ij),k} = 0)}{\binom{|V_c|}{2}} \geq \gamma_2 \in (p_2, 1)$, where

$p_2 = \frac{\sum_{i,j \in V, i < j} I(\hat{\beta}_{(ij),k} \neq 0 | \beta_{(ij),k} = 0)}{\binom{|V|}{2}}$ is the proportion of false positive associations in G . Furthermore, let $m_0, n_0 = \Omega(\max\{m^\epsilon, n^\epsilon\})$ for some $0 < \epsilon < 1$, where Ω denotes a loose lower bound. Then for sufficiently large m, n with $\zeta(\gamma_1, p_1)m_0 \geq 4 \log n(n-1)$, $\zeta(\gamma_1, p_1)n_0(n_0-1) \geq 16 \log m$, and $\zeta(\gamma_2, p_2)n_0 \geq 4 \log n$, we have

$$\begin{aligned} & \mathbb{P}\left(|S_c| \geq m_0, |F_c| \geq \binom{n_0}{2}, |V_c| \geq n_0\right) \\ & \leq 2mn^2(n-1) \cdot \exp\left(-\frac{1}{8}\zeta(\gamma_1, p_1)m_0n_0(n_0-1) - \frac{1}{4}\zeta(\gamma_2, p_2)n_0^2\right), \end{aligned} \quad (6)$$

where $\zeta(a, b) = \left\{\frac{1}{(a-b)^2} + \frac{1}{3(a-b)}\right\}^{-1}$.

Lemma 1 is proved in Appendix B. Lemma 1 states that the probability of identifying a multi-level subgraph of \hat{B}_c composed of false positive associations $\{\hat{\beta}_{(ij),k} \neq 0 | \beta_{(ij),k} = 0\}$ exponentially converges to 0 as the sizes and densities of the multi-level sub-network increase. In practice, the probability of a false positive network with reasonable size (e.g., $|S| \times |F| = 10 \times 10$) and sound densities is less than 10^{-16} . It is very unlikely that false positive FC-SI associations $\{\beta_{(ij),k} \neq 0\}$ would form a large and dense subgraph B_c .

2.5 Inference for extracted \hat{B}_c

Recall from Section 2.3 that our study aims to identify specific subsets of SIs and FCs that exhibit systematic association patterns encoded by B_c . Performing Algorithm 1 returns a collection of such subgraphs \hat{B}_c . Our next goal is to conduct a network-level statistical inference to gauge the significance of each \hat{B}_c with multiple corrections (Goeman et al., 2022; Zhang et al., 2023; Chen et al., 2023). Roughly speaking, we assess the statistical significance of each B_c by testing:

$$\begin{aligned} \mathbb{H}_0 &: B_c \text{ is not a dense multi-level subgraph constituted by associated SI-FC pairs;} \\ \mathbb{H}_a &: B_c \text{ is a dense multi-level subgraph reflecting systematic FC-SI associations.} \end{aligned} \quad (7)$$

More precisely, under \mathbb{H}_0 , the edges of B_c is randomly distributed among all possible pairs. Per Lemma 1, it is rare to observe large and dense multi-level subgraph B_c under the null. Therefore, we can straightforwardly perform the commonly used permutation testing strategy in neuroimaging statistics to assess the significance of \hat{B}_c while controlling the FWER (Zalesky et al. (2010); Nichols (2012); Woo et al. (2014)). However, our testing object is a multi-level subgraph, which is different from the voxel-based ‘‘clusters’’ commonly encountered in conventional cluster-extent inference because the rareness of \hat{B}_c is jointly determined by both the densities and sizes of the dense bipartite and clique of \hat{B}_c instead of a measure of cluster-extent (e.g., the number of voxels). To address this challenge, we propose a novel test statistic $\mathcal{T}(\hat{B}_c)$, proportional to the upper bound of the probability of observing a clique of certain size and density in a random graph, which appeared in (6):

$$\mathcal{T}(\hat{B}_c) = \exp\left(-\frac{1}{4}\zeta(\gamma_1, p_1)|S_c||F_c| - \frac{1}{4}\zeta(\gamma_2, p_2)|V_c|^2\right), \quad (8)$$

where $\zeta(a, b) = \left\{ \frac{1}{(a-b)^2} + \frac{1}{3(a-b)} \right\}^{-1}$, $\gamma_1 = \frac{|H_c|}{|S_c||F_c|}$, $p_1 = \frac{\sum_{k \in S_c, (ij) \in F} I(\hat{\beta}_{(ij), k} \neq 0)}{|S||F|}$, $\gamma_2 = \frac{|F_c|}{\binom{|V_c|}{2}}$, $p_2 = \frac{\sum_{i, j \in V_c, i < j} I(\hat{\beta}_{(ij), k} \neq 0)}{\binom{|V|}{2}}$. We formally present our proposed *network-based permutation test* for the significance of each extracted \hat{B}_c in Algorithm 2. The permutation procedure outlined in Algorithm 2 is effective in simulating the null distribution of the test statistic $T(\hat{B}_c)$. Therefore, FWER can be controlled effectively, yielding a corrected p -value for each extracted \hat{B}_c .

Algorithm 2 Assess the significance of $\{\hat{B}_c\}_{c=1, \dots, C}$

Input: $\{a_{(ij), k}\}, \hat{C} \geq 1, \{\hat{B}_c\}, \alpha$

output: FWER-controlled significance values for each \hat{B}_c

1. Choose a sound cut-off \hat{r} and binarize graph $B[\hat{r}]: B[\hat{r}]_{(ij), k} = I(a_{(ij), k} > \hat{r})$
2. Estimate edge densities for B and G , respectively:

$$\text{Overall density : } \hat{p}_1 = \frac{\sum_{k \in S_c, (ij) \in F} I(a_{(ij), k} > \hat{r})}{|S||F|}, \quad \hat{p}_2 = \frac{\sum_{i, j \in V_c, i < j} f_{ij}}{\binom{|V|}{2}};$$

$$\text{Within-subgraph density : } \hat{\gamma}_1 = \frac{\sum_{k \in \hat{S}_c, (ij) \in \hat{F}_c} I(a_{(ij), k} > \hat{r})}{|\hat{S}_c||\hat{F}_c|}, \quad \hat{\gamma}_2 = \frac{\sum_{i, j \in \hat{V}_c, i < j} f_{ij}}{\binom{|\hat{V}_c|}{2}}.$$

3. Calculate test statistic $\mathcal{T}_0(\hat{B}_c)$ for the current \hat{B}_c
4. Shuffle group labels of data P times and implement MOAT on each shuffled graph
5. Store the maximal test statistic for each simulation $l = 1, \dots, L$:

$$\mathcal{T}_l = \sup_{c=1, \dots, \hat{C}^l} \exp \left(-\frac{1}{4} \zeta \left(\gamma_1^l, p_1^l \right) |\hat{S}_c^l| |\hat{F}_c^l| - \frac{1}{4} \zeta \left(\gamma_2^l, p_2^l \right) |\hat{V}_c^l|^2 \right)$$

6. Calculate the percentile of $\mathcal{T}_0(\hat{B}_c)$ in $\{\mathcal{T}_l\}_{l \in (1, \dots, L)}$ as the FWER q -value and reject \mathbb{H}_0 if $q < \alpha$, where α is a pre-specified significant level
-

Evaluating the joint effect of multiple SIs on FCs. With each $\hat{B}_c = (S_c, F_c)$, we have a set of structural measures $\{X_k, k \in S_c\}$ associated with functional measures $\{Y_{ij}, (ij) \in F_c\}$. However, this does not automatically provide the joint effect (i.e., $\sum_{(ij) \in F_c, k \in S_c} \beta_{(ij), k} X_k$) of the selected SIs on each selected FC measure. To assess the joint effect, we can adopt the existing multivariate-to-multivariate analysis tools (e.g., CCA). Detailed procedures for applying CCA on \hat{B}_c is provided in Appendix D. Alternatively, one can conduct low-rank regression on outcomes and predictors in each \hat{B}_c to estimate the final effect size (Vounou et al., 2010; Wang et al., 2012; Zhu et al., 2014; Kong et al., 2019).

3 Simulation

In this simulation study, we probed whether MOAT can extract informative subgraphs $\{\hat{B}_c\}$ from the multi-level graph B and G with high accuracy and replicability. We evaluate MOAT to finite-sample simulation data under various conditions (e.g., different sample sizes and effect sizes) with comparisons to several commonly used biclustering methods and sCCA-based methods.

3.1 Synthetic data

We generate synthetic FC data $\mathbf{Y}^{(d)} = \{y_{ij}^{(d)}\}_{i,j < n}$ and SI data $\mathbf{X}^{(d)} = (x_1^{(d)}, \dots, x_m^{(d)})^T$ based on the following multivariate Gaussian distribution:

$$\begin{pmatrix} \mathbf{X}^{(d)} \\ \mathbf{Y}^{(d)} \end{pmatrix} \sim N \left[\begin{pmatrix} \boldsymbol{\mu}_X \\ \boldsymbol{\mu}_Y \end{pmatrix}, \begin{pmatrix} \boldsymbol{\Sigma}_{X,X} & \boldsymbol{\Sigma}_{X,Y} \\ \boldsymbol{\Sigma}_{Y,X} & \boldsymbol{\Sigma}_{Y,Y} \end{pmatrix} \right], \quad (9)$$

where $\begin{pmatrix} \boldsymbol{\mu}_X \\ \boldsymbol{\mu}_Y \end{pmatrix}$ is the partitioned mean vector of SI and FC data respectively, and $\boldsymbol{\Sigma} = \begin{pmatrix} \boldsymbol{\Sigma}_{X,X} & \boldsymbol{\Sigma}_{X,Y} \\ \boldsymbol{\Sigma}_{Y,X} & \boldsymbol{\Sigma}_{Y,Y} \end{pmatrix}$ is the partitioned variance-covariance matrix. For simplicity, we set $\begin{pmatrix} \boldsymbol{\mu}_X \\ \boldsymbol{\mu}_Y \end{pmatrix}$ as a zero vector, representing normalized data, while the construction of $\boldsymbol{\Sigma}$ depends on two key factors: the multi-level network structure and effect sizes (i.e., FC-SI association strength). Both of these factors are elaborated upon in the following paragraph.

In this simulation, we consider 500 SIs and 4950 FCs, where the FC measures are calculated based on a brain network with 100 regions, resulting in $\binom{100}{2} = 4950$ pairwise connectivity values. To determine the network structure for $\boldsymbol{\Sigma}$, we consider the following multi-level graph consisting of (i) a bipartite graph $B = (S, F; H)$ depicting the FC-SI associations, where $|S| = 500$, $|F| = 4950$; (ii) a unipartite graph $G = (V; E)$ depicting the brain functional connectome, where $|V| = 100$. Specially, we generate two sub-networks within B , denoted as B_1 and B_2 , characterized by higher FC-SI partial correlations ρ_1 and ρ_2 than the rest of B . B_1 consists of 40 SI measures and 435 FC measures, where the 435 FC measures collectively compose a functional connectome G_1 of 30 brain regions; B_2 consists of 60 SI measures and 190 FC measures, where the 190 FC measures collectively compose another functional connectome G_2 of 20 brain regions. For a visual representation of these two sub-networks, please refer to the graph illustration in [Figure 3](#).

Built on this network architecture, we configure the covariance matrix $\boldsymbol{\Sigma}$ such that $\rho_1, \rho_2 > \rho_0$ to emulate different effect sizes. Here, we set $\rho_0 = 0.15$ as the partial correlation of FC-SI edges outside of B_1 and B_2 . Next, by correlating the FC and SI data simulated from (9) using the aforespecified $\begin{pmatrix} \boldsymbol{\mu}_X \\ \boldsymbol{\mu}_Y \end{pmatrix}$ and $\boldsymbol{\Sigma}$, we obtain an FC-SI association matrix $\mathbf{A}_{500 \times 4950}$. \mathbf{A} governs the edge variable H in the bipartite graph $B = (S, F; H)$ by $h_{(ij),k} = I(a_{(ij),k} > r)$, where r is a pre-selected threshold for correlation strength. Lastly, to assess MOAT performance under different settings, three configurations of $(\rho_0, \rho_1, \rho_2; D)$ are simulated: $(0.15, 0.55, 0.60; 200)$, $(0.15, 0.60, 0.45; 300)$, and $(0.15, 0.70, 0.40; 400)$, where D represents the sample size as defined previously. For each configuration, we simulate 500 repeated data sets $\{\mathbf{A}^l\}_{l \in \{1, \dots, 500\}}$ to better access accuracy and replicability of MOAT.

3.2 Performance evaluation

For each simulated dataset, we apply MOAT to estimate the multi-level sub-networks \hat{B}_c containing strong FC-SI associations and perform our proposed network-based permutation test outlined in [Algorithm 2](#) on \mathbf{A}^l . Regarding B_c extraction and $\{\beta_{(ij),k} \neq 0\}$ identification, we benchmark MOAT against a few popular approaches including (i) three biclustering methods that are commonly used for sub-network detection: Bipartite Spectral Graph Partitioning (BSGP) ([Wieling and Nerbonne, 2009](#)), Information Theoretic Learning (ITL) ([Erdogmus, 2002](#)), and Factor Analysis for Bicluster

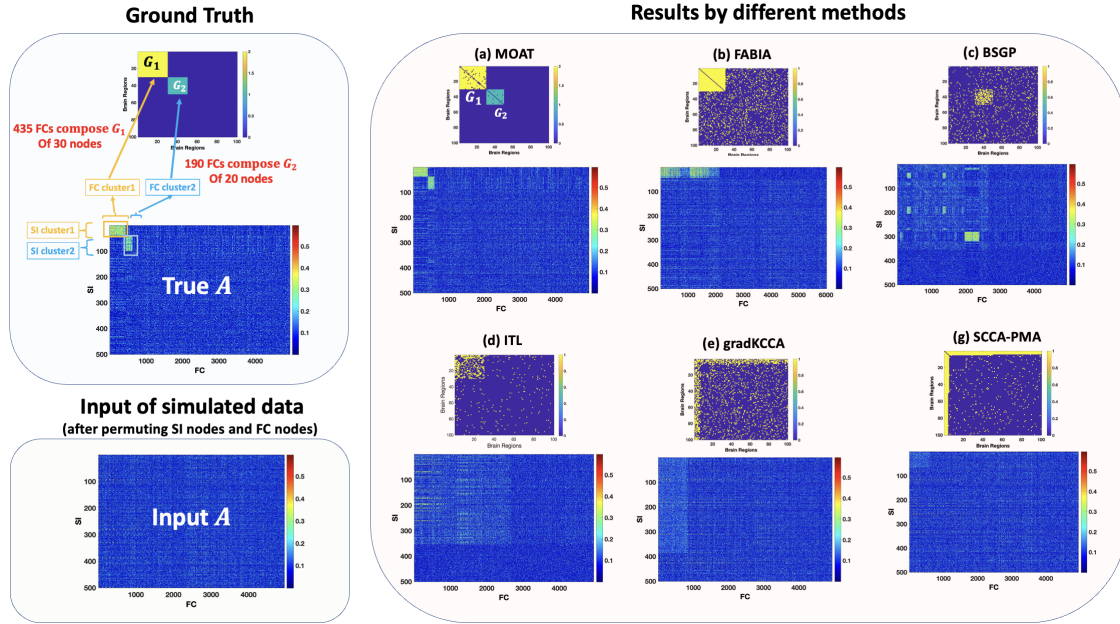


Figure 3: Applying MOAT and comparative methods to an inference matrix $A_{500 \times 4950}$ with sample size $D = 200$. $A_{500 \times 4950}$ is simulated to store partial correlations between 500 SI measures and 4950 FC measures, where the 4950 FC measures are obtained from region-wise functional connections between 100 brain regions. Two sub-networks B_1 and B_2 with FC-SI partial correlations $(\rho_1, \rho_2) = (0.40, 0.35)$ are generated within B , while the partial correlations for the rest of B are set to be $\rho_0 = 0.15$. The right panel shows the results of applying MOAT, biclustering and sCCA methods. Both MOAT and biclustering methods are more accurate in revealing sub-network patterns than sCCA methods since they incorporate cluster/network information. When jointly evaluating TPR and TNR, MOAT outperforms other methods, as TPR and TNR rely heavily on accurate sub-network extraction and inference.

$(\rho_1, \rho_2; D)$	measures	metrics	MOAT	BGSP	ITL	FABIA	gradKCCA	SCCA-PMA
(0.55, 0.60; 200)	SI	TPR	1 (0)	0.4767 (0.1357)	0.4010 (0.4169)	0.5768 (0.1019)	0.3450 (0.0376)	0.4309 (0.0147)
		TNR	0.9844 (0.0129)	0.9492 (0.0290)	0.9560 (0.0430)	0.7243 (0.0506)	0.4793 (0.0175)	0.6119 (0.0152)
	FC	TPR	0.9358 (0.0456)	0.4549 (0.0512)	0.4547 (0.0498)	0.8291 (0.0718)	0.4024 (0.0065)	0.5109 (0.0032)
		TNR	1 (0)	0.9462 (0.0129)	0.8683 (0.1423)	0.8288 (0.0263)	0.5547 (0.0076)	0.6643 (0.0047)
	SI-FC pair	TPR	0.9358 (0.0456)	0.4090 (0.0184)	0.3891 (0.0267)	0.4275 (0.0578)	0.3417 (0.0138)	0.4110 (0.0038)
		TNR	0.9844 (0.0129)	0.9082 (0.0333)	0.7352 (0.3918)	0.6491 (0.0814)	0.4528 (0.0911)	0.5834 (0.0124)
(0.60, 0.40; 300)	SI	TPR	1 (0)	0.4760 (0.1393)	0.3734 (0.3464)	0.5165 (0.1037)	0.3790 (0.0336)	0.3202 (0.0138)
		TNR	0.9761 (0.0253)	0.9540 (0.0309)	0.9547 (0.0786)	0.6953 (0.0636)	0.4350 (0.0168)	0.5375 (0.0142)
	FC	TPR	0.8815 (0.1480)	0.4571 (0.0572)	0.3557 (0.0542)	0.8048 (0.0097)	0.3888 (0.0069)	0.5103 (0.0031)
		TNR	1 (0)	0.9480 (0.0126)	0.9026 (0.1149)	0.8291 (0.0035)	0.4734 (0.0072)	0.5646 (0.0073)
	SI-FC pair	TPR	0.8815 (0.1480)	0.4101 (0.0245)	0.3552 (0.0262)	0.4069 (0.0127)	0.3492 (0.0168)	0.4047 (0.0035)
		TNR	0.9761 (0.0253)	0.9045 (0.0352)	0.7797 (0.3163)	0.6694 (0.0083)	0.3361 (0.0112)	0.5907 (0.0104)
(0.70, 0.45; 400)	SI	TPR	1 (0)	0.4649 (0.1278)	0.3507 (0.3737)	0.5677 (0.0094)	0.3956 (0.0512)	0.4009 (0.0188)
		TNR	0.9800 (0.0202)	0.9443 (0.0549)	0.9493 (0.1036)	0.7533 (0.0742)	0.4423 (0.0231)	0.6255 (0.0186)
	FC	TPR	0.9073 (0.1098)	0.4621 (0.0731)	0.3831 (0.0938)	0.8094 (0.0502)	0.3940 (0.0181)	0.5803 (0.0031)
		TNR	1 (0)	0.9112 (0.0047)	0.8568 (0.1952)	0.8073 (0.0327)	0.4245 (0.0175)	0.6479 (0.0056)
	SI-FC pair	TPR	0.9073 (0.0202)	0.4248 (0.0615)	0.3378 (0.0572)	0.8048 (0.0097)	0.4212 (0.0246)	0.4917 (0.0042)
		TNR	0.9800 (0.0202)	0.9055 (0.0442)	0.7939 (0.4354)	0.6730 (0.0996)	0.3317 (0.0328)	0.5660 (0.0238)
Computational Time (MATLAB, 6-Core Intel Core i5, 32 GB RAM)			2min	5min	22min	2min	1min	2min

Table1: Inference results of MOAT and comparative methods under different settings. ρ_1, ρ_2 denote the partial correlations between SI and FC measures in the dense sub-networks B_1 and B_2 , respectively, and D denotes the sample size. We summarize the means (standard deviations) of the TPR and TNR for identified SIs, FCs, and FC-SI pairs based on 500 repeated simulations. The results show that MOAT outperforms the compared methods under different scenarios, indicating its effectiveness in identifying the correct dense sub-networks with true positive FC-SI associated pairs.

Information Acquisition (FABIA) (Hochreiter et al., 2010); (ii) two sCCA-based methods that identify and measure the associations between two canonical/latent types of variables: a Large-Scale Sparse Kernel Canonical Correlation method proposed by Uurtio et al. (2019), and sCCA through a penalized matrix decomposition (sCCA-PMA) proposed by Witten et al. (2009).

We evaluate methods’ performance by assessing the deviation of the estimated \hat{B}_c from true B_c at both node-level, and edge-level (i.e., $\hat{\beta}_{(ij),k} \neq 0$ v.s true $\beta_{(ij),k} \neq 0$). Specifically, we consider the comparisons from the following three perspectives: SI variable selection, FC variable selection, and FC-SI pair selection. We use true positive rate (TPR) and true negative rate (TNR) as the evaluation criteria for both node-level and edge-level deviations. TPR is determined by the proportion of FC/SI nodes or FC-SI edges in B_c that can be recovered by \hat{B}_c ; TNR is determined by the proportion of FC/SI nodes or FC-SI edges in B/B_c that can be recovered by B/\hat{B}_c .

Figure 3 provides a graphical overview of the performance of each method. Table 1 demonstrates the performance of all methods under multiple settings. The TPR and TNR are determined by the accuracy of both sub-network extraction and network-level inference. In general, both MOAT and biclustering-based methods can recover sub-network patterns more accurately than sCCA-based methods because the network structures of FC-SI association patterns can be better recognized. Under different settings, MOAT can detect the target sub-networks with high sensitivity with few or none false-positive FC-SI edges because the cost of removing a true positive association or including a false positive edge is very high, as regulated by objective function (5). The performance of biclustering methods is also improved with increased effect sizes with low false positive rates and medium to low sensitivity. In contrast, sCCA-based methods is invariant to different effect sizes, and may miss the underlying FC-SI association patterns due to various noise.

Overall, MOAT is robust to noise and sensitive to organized FC-SI association patterns. MOAT outperforms comparable biclustering and sCCA methods under different settings, especially when systematic FC-SI association patterns are present. This superiority stems from MOAT’s ability to accurately extract FC-SI association patterns through multi-level sub-network analysis and tailored sub-network-level inference.

4 Study of FC-SI associations in brain connectome data

4.1 UK Biobank sample and neuroimaging data

We aim to investigate the systematic effects of certain structural brain imaging measures on the functional connectome using UK Biobank data (Sudlow et al., 2015). The UK Biobank is a vast biomedical database with approximately half a million participants from the UK, where a total of 40,923 healthy individuals were found to have usable resting-state fMRI (rs-fMRI) data that passed quality control (Alfaro-Almagro et al., 2018). Among them, a subgroup of 4,242 individuals possessed complete data on the following three sets of measurements we have chosen to focus on in this study:

- (i) *105 SI measures*: we collected 105 SI variables including 39 white matter integrity measures and 66 cortical thickness measures. The white matter integrity reflects the overall health and coherence of brain white matter and was assessed by fractional anisotropy (FA) obtained from DTI data in this study. The DTI data was pre-processed using ENIGMA DTI protocols

(Jahanshad et al., 2013) and white matter tracts were labeled based on the JHU ICBM DTI-81 Atlas (Smith et al., 2006; Mori et al., 2008). A complete list of the 39 regional white matter tracts can be found in Appendix C.3. On the other hand, cortical thickness measures gauge the width of the gray matter of the human cortex, and were obtained from T1 MRI and labeled based on the FreeSurfer atlas (Tustison et al., 2014).

- (ii) *30,135 FC measures*: functional connectome data were obtained from rs-fMRI data based on Brainnetome Atlas (Fan et al., 2016). We first performed rs-fMRI preprocessing for all participants and then extracted the averaged time series of blood-oxygen-level-dependent (BOLD) signals from 246 functional brain regions, resulting in $\binom{246}{2} = 30,135$ region-pair FC measures. Details of imaging acquisition and fMRI preprocessing are provided in Appendix C.1.
- (iii) *4 confounding variables*: we adjusted four confounding variables including age (years: 61.46 ± 7.40), sex (M/F: 2003/2239), educational level (years: 17.37 ± 3.92), and body mass index (BMI) (kg/m^2 : 26.35 ± 4.30). These variables have been used in previous neuroimaging literature on studying brain functional connectivity (Miller et al., 2016; Alfaro-Almagro et al., 2021; Bischof and Park, 2015; Agustí et al., 2018).

4.2 Results

We applied MOAT to the multimodal imaging data from the qualified 4,242 UK Biobank participants. First, we obtained the FC-SI association inference matrix $\mathbf{A}_{105 \times 30135}$. Each entry in \mathbf{A} is $a_{(ij),k} = -\log(p_{(ij),k})$, where $p_{(ij),k}$ represents the p -value testing the association between the k -th SI measure and the FC outcome between two brain regions i and j . Next, we performed a hard-thresholding sparsity constraint by setting $a_{(ij),k} = a_{(ij),k} I(a_{(ij),k} < \epsilon)$ for some positive integer ϵ (Zhang et al., 2023). We then applied our proposed greedy peeling algorithm 1 to the inference matrix \mathbf{A} , with tuning parameters $\lambda_1 = 1.25, \lambda_2 = 1.5$ selected by the KL divergence with a mixed Bernoulli distribution based on random graphs B and G . Algorithm 1 returned one multi-level sub-network $\hat{B}_1 \in B$. Lastly, we performed the network-level statistical inference on \hat{B}_1 using Algorithm 2. The testing results showed that the systematic association pattern of \hat{B}_1 is statistically significant ($p < 0.0001$).

Specifically, results show that \hat{B}_1 comprised $|S_1| = 23$ SI measures and $|F_1| = 1316$ FC outcomes, as highlighted in Figure 5(b). Furthermore, the extracted $|F_1|$ unfolded into a dense clique $\hat{G}_1 \in G$ consisting of $|V_1| = 79$ regions, as illustrated in Figure 5(e). The FC-SI pairs within the identified sub-network \hat{B}_1 demonstrate significantly stronger associations compared to those outside of the network, as evidenced by the high R^2 and t -statistics shown in Figure 5 (c-d). The 23 extracted SI measures consist of 3 cortical thickness measures and 20 FAs: the three cortical thickness measures correspond to the mean thickness of the parahippocampal, superior temporal, and cuneus gyrus; while for the 20 FA measures extracted, the top four with the strongest FC associations are CST-R (corticospinal tract, right hemisphere), CST-L (corticospinal tract, left hemisphere), ICP (inferior cerebellar peduncles), and FX (fornix). More detailed information about the remaining 16 FA measures can be found in Appendix E.3. Figure 6 (left panel) illustrates the names and spatial locations of the 20 selected FAs.

The right panel in Figure 6 shows the spatial distributions of within- \hat{B}_1 brain regions (79 regions in total), where they are predominantly located in six cortices: frontal, subcortical, temporal,

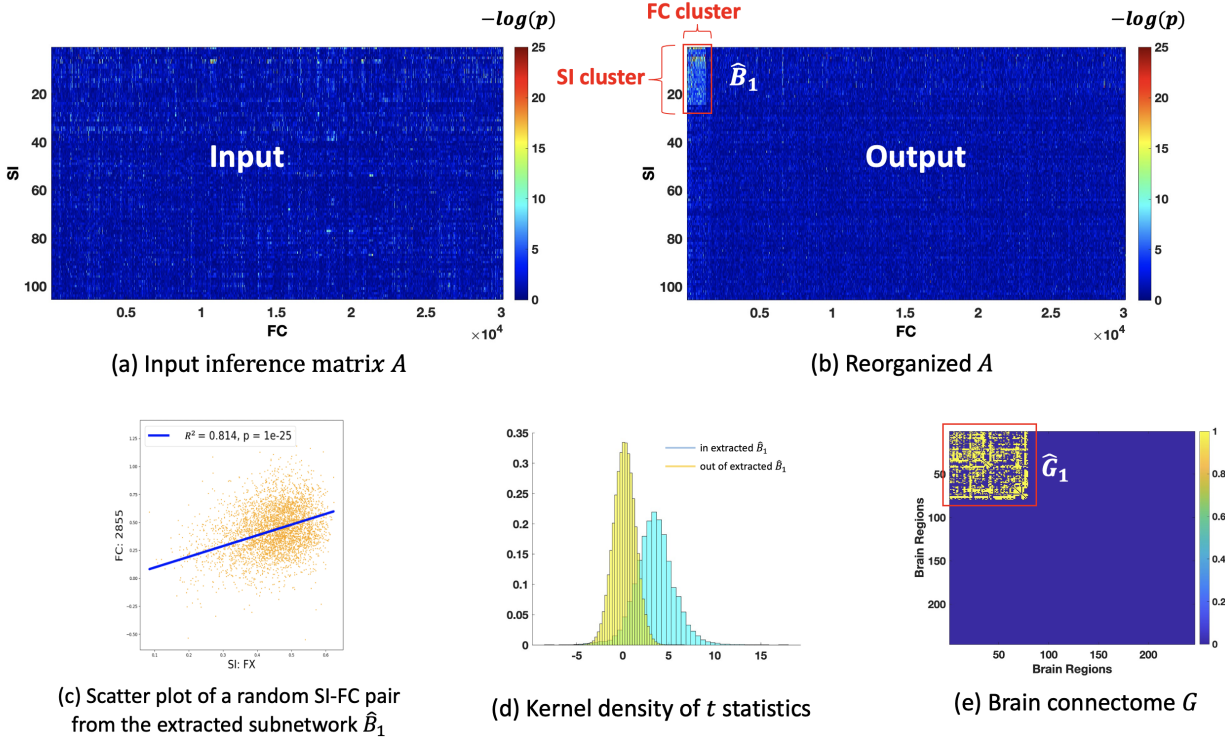


Figure 5: Application of MOAT on a real neuroimaging dataset obtained from the UK Biobank. (a) shows a heatmap of the inference matrix $A_{105 \times 30135}$. Each element is a $-\log(p)$ value testing the association between SI and FC measures. (b) shows a heatmap of a reorganized A with element in the detected subgraph \hat{B}_1 pushed to the top left corner. Within the second level G composed by the selected FCs, there exists an organized subgraph $\hat{G}_1 \subset G$ revealed in (e). As shown in (c) and (d), the FC-SI pairs within the identified \hat{B}_1 have significantly stronger associations compared to those outside of the network.

parietal, insular, and limbic. Moreover, these regions consist of several well-defined brain functional networks including temporo-frontal, somatomotor, ventral attention, frontoparietal, and (partial) default mode network (DMN). Overall, Figure 6 provides a 3D demonstration showcasing the systematic association patterns between the subsets of SIs and FCs revealed by MOAT. Notably, both the FC-SI significantly associated sub-network (\hat{B}_1) and the brain functional sub-connectome (\hat{G}_1) exhibit well-organized topological structures.

We further applied CCA on the extracted sub-network \hat{B}_1 to quantitatively measure the canonical associations among the FC-SI pairs within \hat{B}_1 . Results showed that the sample canonical correlations of the first three canonical variate pair in \hat{B}_1 were 0.81, 0.69, and 0.68 respectively. In contrast, we performed sparse CCA proposed by Witten et al. (2009) on the full graph B and G , given the ultra high dimensionality of data. This yielded sample canonical correlations of 0.18, 0.15, and 0.14 for the first three canonical variate pairs, respectively. Notably, MOAT can better recognize the underlying large-scale FC-SI association patterns and then provide an improved estimation of the multivariate-to-multivariate association.

In summary, the application of MOAT helps to unfold the complex yet systematic and strong interplay between subsets of structural and functional measures of the human brain. Our findings suggest i) FC-SI associations are highly concentrated in a subset of SIs and FC sub-networks

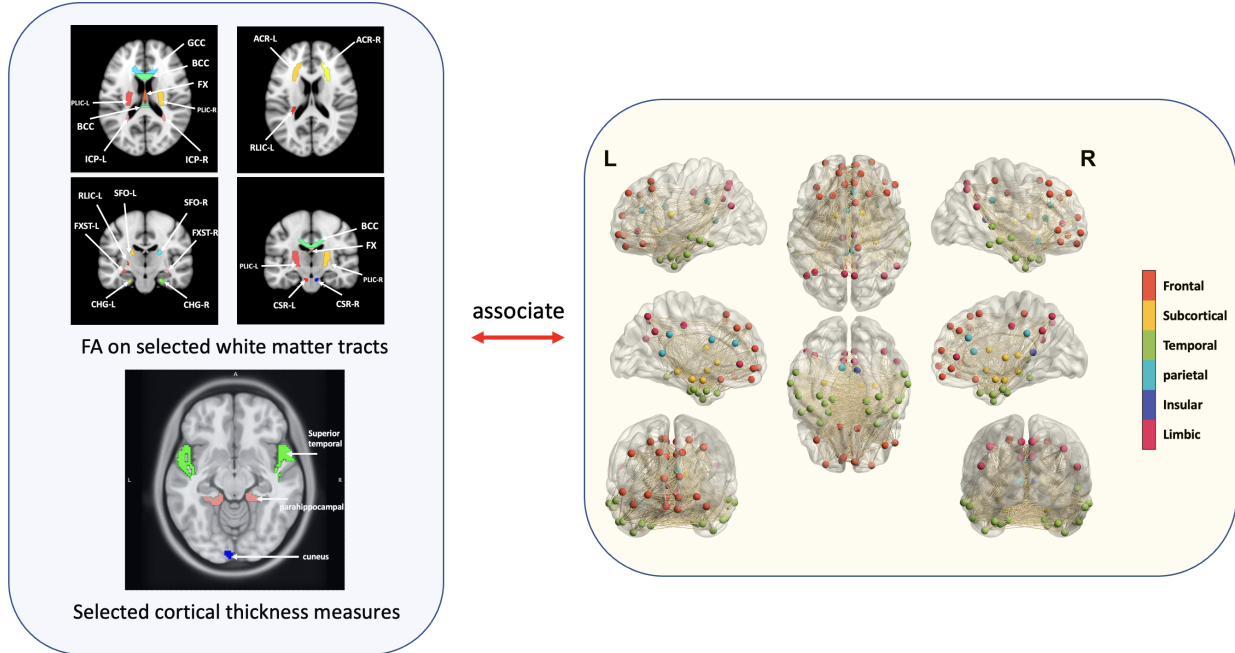


Figure 6: *Extracted FC-SI associated sub-networks by MOAT, adjusted for age, sex, educational level, and BMI. Specifically, the left panel shows the SI cluster in the extracted sub-networks, which contains 20 FA measures and 3 cortical thickness measures. The top four FA measures with remarkably stronger associations with the detected FC sub-network are CST-R, CST-L, ICP, and FX. The three selected cortical thickness measures correspond to the mean thickness of the parahippocampal, superior temporal, and cuneus gyrus. The right panel shows the detected FC sub-network that is strongly impacted by the 23 selected SIs. The detected FC sub-network covers 79 brain regions and composes several high-level cognitive brain networks including the default mode network, temporo-frontal network, somatomotor, ventral attention, and frontoparietal network.*

rather than exhibiting a whole-brain diffuse distribution pattern; ii) several FC sub-networks are primarily influenced by white matter integrity measures (refer to Table 2 in Appendix E.3 for possible mapping relationships); iii) multiple SI measures jointly affect the overall FC outcomes based on MOAT-guided CCA analysis. While, on a high level, our results align well with previous medical findings (Cheung et al., 2008; Pradat and Dib, 2009; Chaddock-Heyman et al., 2013; Corrigan et al., 2015), MOAT reveals more refined patterns with improved spatial specificity and biological interpretability.

5 Discussion

Our newly developed approach, MOAT, offers a novel strategy to investigate the complex association patterns between multimodal neuroimaging data with matrix-outcomes (FCs) and a vector of imaging predictors (SIs). MOAT deciphers the complex FC-SI association patterns in a multi-level graph structure revealing the joint effect of a small set of SI predictors on FC sub-networks. The multi-level graph structure can effectively reduce the number of parameters while preserving the spatial specificity of FCs and SIs. MOAT delivers findings in organized multi-level sub-networks largely suppressing individual false positive FC-SI associations (see Lemma 1 in section 2.4). We

Table. 20 selected white matter tracts strongly associated with identified FC sub-network

Region	Abbreviation	Category	Function
Inferior cerebellar peduncle	ICP	Brainstem	coordination of movement and proprioceptive
Genu of corpus callosum	GCC	Commissural	information transmission; movement
Body of corpus callosum	BCC	Commissural	control; cognitive functions; vision
Fornix	FX	Association	memory formation and retrieval
Corticospinal tract R	CST-L	Brainstem	Motor signal transmission; voluntary
Corticospinal tract L	CST-R	Brainstem	muscle control
Posterior limb of internal capsule R	PLIC-R	Projection	sense; motor; information flow past the
Posterior limb of internal capsule L	PLIC-L	Projection	basal ganglia
Retrolemniscal part of internal capsule L	RLIC-L	Projection	
Anterior corona radiata R	ACR-R	Projection	voluntary emotional expression; sensory
Anterior corona radiata L	ACR-L	Projection	input
Cingulum hippocampus R	CHG-R	Association	Affect; response selection in skeletomotor
Cingulum hippocampus L	CHG-L	Association	control; visuospatial processing and memory access
Fornix (cres)/stria terminalis R	FXST-R	Association	Memory; emotion, regulation of stress
Fornix (cres)/stria terminalis L	FXST-L	Association	responses within the brain
Superior fronto-occipital fasciculus R	SFO-R	Association	Auditory verbal and declarative
Superior fronto-occipital fasciculus L	SFO-L	Association	
Uncinate fasciculus R	UN-R	Association	Memory; language; emotion
Tapetum R	TAP-R	Commissural	information transmission; visual
Tapetum L	TAP-L	Commissural	capabilities

Table 2: 20 selected white matter tracts strongly associated with identified FC sub-network

developed computationally efficient algorithms to extract multi-level sub-networks. We further showed the consistency of the MOAT method. In addition, we develop a tailored network-level inference approach to test the extracted multi-level sub-networks while controlling FWER. Last, MOAT is also compatible with existing multivariate-to-multivariate analysis tools (e.g., CCA).

In our case study, we investigated the FC-SI associations based on a large sample and revealed systematic association patterns with neurological explanations. This may enhance our understanding of how the brain structure and function interactively work during resting states and may lead to insights that can guide future cognitive and psychiatric therapy. However, since UK biobank participants mainly consist of elder Caucasians, our conclusion may be limited. Further investigation and integrated analysis is required to gain more comprehensive understanding of the FC-SI associations. The software package for MOAT is available at <https://github.com/TongLu-bit/MultilayerNetworks-MOAT>.

Declaration of interest: none.

Acknowledgments

Tong Lu and Shuo Chen were supported by the National Institutes of Health under Award Numbers 1DP1DA04896801, EB008432, and EB008281. Yuan Zhang was supported by the National Science Foundation under Award Number DMS-2311109.

References

- Agustí, A., García-Pardo, M. P., López-Almela, I., Campillo, I., Maes, M., Romani-Pérez, M., and Sanz, Y. (2018). Interplay between the gut-brain axis, obesity and cognitive function. Frontiers in neuroscience, 12:155.
- Alfaro-Almagro, F., Jenkinson, M., Bangarter, N. K., Andersson, J. L., Griffanti, L., Douaud, G., Sotiropoulos, S. N., Jbabdi, S., Hernandez-Fernandez, M., Vallee, E., et al. (2018). Image processing and quality control for the first 10,000 brain imaging datasets from uk biobank. Neuroimage, 166:400–424.
- Alfaro-Almagro, F., McCarthy, P., Afyouni, S., Andersson, J. L., Bastiani, M., Miller, K. L., Nichols, T. E., and Smith, S. M. (2021). Confound modelling in uk biobank brain imaging. NeuroImage, 224:117002.
- Bahrami, M., Laurienti, P. J., and Simpson, S. L. (2019). Analysis of brain subnetworks within the context of their whole-brain networks. Human brain mapping, 40(17):5123–5141.
- Bai, F., Zhang, Z., Watson, D. R., Yu, H., Shi, Y., Yuan, Y., Qian, Y., and Jia, J. (2009). Abnormal integrity of association fiber tracts in amnesic mild cognitive impairment. Journal of the neurological sciences, 278(1-2):102–106.
- Ball, G., Aljabar, P., Nongena, P., Kennea, N., Gonzalez-Cinca, N., Falconer, S., Chew, A. T., Harper, N., Wurie, J., Rutherford, M. A., et al. (2017). Multimodal image analysis of clinical influences on preterm brain development. Annals of neurology, 82(2):233–246.

- Bischof, G. N. and Park, D. C. (2015). Obesity and aging: Consequences for cognition, brain structure and brain function. Psychosomatic medicine, 77(6):697.
- Bowman, F. D., Zhang, L., Derado, G., and Chen, S. (2012). Determining functional connectivity using fmri data with diffusion-based anatomical weighting. NeuroImage, 62(3):1769–1779.
- Buckner, R. L., Andrews-Hanna, J. R., and Schacter, D. L. (2008). The brain’s default network: anatomy, function, and relevance to disease. Annals of the new York Academy of Sciences, 1124(1):1–38.
- Bullmore, E. and Sporns, O. (2009). Complex brain networks: graph theoretical analysis of structural and functional systems. Nature reviews neuroscience, 10(3):186–198.
- Cao, M., Wang, J.-H., Dai, Z.-J., Cao, X.-Y., Jiang, L.-L., Fan, F.-M., Song, X.-W., Xia, M.-R., Shu, N., Dong, Q., et al. (2014). Topological organization of the human brain functional connectome across the lifespan. Developmental cognitive neuroscience, 7:76–93.
- Chachlakis, D. G., Prater-Bennette, A., and Markopoulos, P. P. (2019). L1-norm tucker tensor decomposition. IEEE Access, 7:178454–178465.
- Chaddock-Heyman, L., Erickson, K. I., Voss, M. W., Powers, J. P., Knecht, A. M., Pontifex, M. B., Drollette, E. S., Moore, R. D., Raine, L. B., Scudder, M. R., et al. (2013). White matter microstructure is associated with cognitive control in children. Biological psychology, 94(1):109–115.
- Chekuri, C., Quanrud, K., and Torres, M. R. (2022). Densest subgraph: Supermodularity, iterative peeling, and flow. In Proceedings of the 2022 Annual ACM-SIAM Symposium on Discrete Algorithms (SODA), pages 1531–1555. SIAM.
- Chen, S., Zhang, Y., Wu, Q., Bi, C., Kochunov, P., and Hong, L. E. (2023). Identifying covariate-related subnetworks for whole-brain connectome analysis. Biostatistics, page kxad007.
- Cheung, V., Cheung, C., McAlonan, G., Deng, Y., Wong, J., Yip, L., Tai, K., Khong, P., Sham, P., and Chua, S. (2008). A diffusion tensor imaging study of structural dysconnectivity in never-medicated, first-episode schizophrenia. Psychological medicine, 38(6):877–885.
- Corrigan, F., Grand, D., and Raju, R. (2015). Brainspotting: Sustained attention, spinothalamic tracts, thalamocortical processing, and the healing of adaptive orientation truncated by traumatic experience. Medical Hypotheses, 84(4):384–394.
- Craddock, R. C., Jbabdi, S., Yan, C.-G., Vogelstein, J. T., Castellanos, F. X., Di Martino, A., Kelly, C., Heberlein, K., Colcombe, S., and Milham, M. P. (2013). Imaging human connectomes at the macroscale. Nature methods, 10(6):524–539.
- Drevets, W. C., Price, J. L., and Furey, M. L. (2008). Brain structural and functional abnormalities in mood disorders: implications for neurocircuitry models of depression. Brain structure and function, 213:93–118.
- Erdogmus, D. (2002). Information theoretic learning: Renyi’s entropy and its applications to adaptive system training. University of Florida.

- Fan, L., Li, H., Zhuo, J., Zhang, Y., Wang, J., Chen, L., Yang, Z., Chu, C., Xie, S., Laird, A. R., et al. (2016). The human brainnetome atlas: a new brain atlas based on connectional architecture. Cerebral cortex, 26(8):3508–3526.
- Fornito, A., Zalesky, A., and Bullmore, E. (2016). Fundamentals of brain network analysis. Academic press.
- Goeman, J. J., Górecki, P., Monajemi, R., Chen, X., Nichols, T. E., and Weeda, W. (2022). Cluster extent inference revisited: quantification and localization of brain activity. arXiv preprint arXiv:2208.04780.
- Hayden, E. P., Wiegand, R. E., Meyer, E. T., Bauer, L. O., O’connor, S. J., Nurnberger Jr, J. I., Chorlian, D. B., Porjesz, B., and Begleiter, H. (2006). Patterns of regional brain activity in alcohol-dependent subjects. Alcoholism: Clinical and Experimental Research, 30(12):1986–1991.
- Hochreiter, S., Bodenhofer, U., Heusel, M., Mayr, A., Mittrecker, A., Kasim, A., Khamiakova, T., Van Sanden, S., Lin, D., Talloen, W., et al. (2010). Fabia: factor analysis for bicluster acquisition. Bioinformatics, 26(12):1520–1527.
- Honey, C. J., Thivierge, J.-P., and Sporns, O. (2010). Can structure predict function in the human brain? Neuroimage, 52(3):766–776.
- Hotelling, H. (1933). Analysis of a complex of statistical variables into principal components. Journal of educational psychology, 24(6):417.
- Jahanshad, N., Kochunov, P. V., Sprooten, E., Mandl, R. C., Nichols, T. E., Almasy, L., Blangero, J., Brouwer, R. M., Curran, J. E., de Zubicaray, G. I., et al. (2013). Multi-site genetic analysis of diffusion images and voxelwise heritability analysis: A pilot project of the enigma-dti working group. Neuroimage, 81:455–469.
- Johnson, D. and Sinanovic, S. (2001). Symmetrizing the kullback-leibler distance. IEEE Transactions on Information Theory.
- Jolliffe, I. T. and Cadima, J. (2016). Principal component analysis: a review and recent developments. Philosophical transactions of the royal society A: Mathematical, Physical and Engineering Sciences, 374(2065):20150202.
- Kemmer, P. B., Wang, Y., Bowman, F. D., Mayberg, H., and Guo, Y. (2018). Evaluating the strength of structural connectivity underlying brain functional networks. Brain Connectivity, 8(10):579–594.
- Kong, D., An, B., Zhang, J., and Zhu, H. (2019). L2rm: Low-rank linear regression models for high-dimensional matrix responses. Journal of the American Statistical Association.
- Lasky-Su, J., Neale, B. M., Franke, B., Anney, R. J., Zhou, K., Maller, J. B., Vasquez, A. A., Chen, W., Asherson, P., Buitelaar, J., et al. (2008). Genome-wide association scan of quantitative traits for attention deficit hyperactivity disorder identifies novel associations and confirms candidate gene associations. American Journal of Medical Genetics Part B: Neuropsychiatric Genetics, 147(8):1345–1354.

- Li, Y., Long, J., He, L., Lu, H., Gu, Z., and Sun, P. (2012). A sparse representation-based algorithm for pattern localization in brain imaging data analysis. *PloS one*, 7(12):e50332.
- Lin, D., Zhang, J., Li, J., Calhoun, V. D., Deng, H.-W., and Wang, Y.-P. (2013). Group sparse canonical correlation analysis for genomic data integration. *BMC bioinformatics*, 14(1):1–16.
- Lu, T., Zhang, Y., Kochunov, P., Hong, E., and Chen, S. (2023). Network method for voxel-pair-level brain connectivity analysis under spatial-contiguity constraints. *arXiv preprint arXiv:2305.01596*.
- Marek, S., Tervo-Clemmens, B., Calabro, F. J., Montez, D. F., Kay, B. P., Hatoum, A. S., Donohue, M. R., Foran, W., Miller, R. L., Hendrickson, T. J., et al. (2022). Reproducible brain-wide association studies require thousands of individuals. *Nature*, 603(7902):654–660.
- Margulis, L. and Sagan, D. (2000). *What is life?* Univ of California Press.
- Mbatchou, J., Barnard, L., Backman, J., Marcketta, A., Kosmicki, J. A., Ziyatdinov, A., Benner, C., O’Dushlaine, C., Barber, M., Boutkov, B., et al. (2021). Computationally efficient whole-genome regression for quantitative and binary traits. *Nature genetics*, 53(7):1097–1103.
- Mihalik, A., Chapman, J., Adams, R. A., Winter, N. R., Ferreira, F. S., Shawe-Taylor, J., Mourão-Miranda, J., Initiative, A. D. N., et al. (2022). Canonical correlation analysis and partial least squares for identifying brain-behaviour associations: a tutorial and a comparative study. *Biological Psychiatry: Cognitive Neuroscience and Neuroimaging*.
- Miller, K. L., Alfaro-Almagro, F., Bangarter, N. K., Thomas, D. L., Yacoub, E., Xu, J., Bartsch, A. J., Jbabdi, S., Sotiropoulos, S. N., Andersson, J. L., et al. (2016). Multimodal population brain imaging in the uk biobank prospective epidemiological study. *Nature neuroscience*, 19(11):1523–1536.
- Mori, S., Oishi, K., Jiang, H., Jiang, L., Li, X., Akhter, K., Hua, K., Faria, A. V., Mahmood, A., Woods, R., et al. (2008). Stereotaxic white matter atlas based on diffusion tensor imaging in an icbm template. *Neuroimage*, 40(2):570–582.
- Nichols, T. E. (2012). Multiple testing corrections, nonparametric methods, and random field theory. *Neuroimage*, 62(2):811–815.
- Pradat, P.-F. and Dib, M. (2009). Biomarkers in amyotrophic lateral sclerosis: facts and future horizons. *Molecular diagnosis & therapy*, 13:115–125.
- Schaid, D. J., Chen, W., and Larson, N. B. (2018). From genome-wide associations to candidate causal variants by statistical fine-mapping. *Nature Reviews Genetics*, 19(8):491–504.
- Smith, S. M., Jenkinson, M., Johansen-Berg, H., Rueckert, D., Nichols, T. E., Mackay, C. E., Watkins, K. E., Ciccarelli, O., Cader, M. Z., Matthews, P. M., et al. (2006). Tract-based spatial statistics: voxelwise analysis of multi-subject diffusion data. *Neuroimage*, 31(4):1487–1505.
- Smith, S. M., Jenkinson, M., Woolrich, M. W., Beckmann, C. F., Behrens, T. E., Johansen-Berg, H., Bannister, P. R., De Luca, M., Drobnjak, I., Flitney, D. E., et al. (2004). Advances in functional and structural mr image analysis and implementation as fsl. *Neuroimage*, 23:S208–S219.

- Sudlow, C., Gallacher, J., Allen, N., Beral, V., Burton, P., Danesh, J., Downey, P., Elliott, P., Green, J., Landray, M., et al. (2015). Uk biobank: an open access resource for identifying the causes of a wide range of complex diseases of middle and old age. PLoS medicine, 12(3):e1001779.
- Sun, D., Rakesh, G., Haswell, C. C., Logue, M., Baird, C. L., O’Leary, E. N., Cotton, A. S., Xie, H., Tamburrino, M., Chen, T., et al. (2022). A comparison of methods to harmonize cortical thickness measurements across scanners and sites. Neuroimage, 261:119509.
- Tang, Y., Liu, X., Wang, J., Li, M., Wang, Q., Tian, F., Su, Z., Pan, Y., Liu, D., Lipka, A. E., et al. (2016). Gapit version 2: an enhanced integrated tool for genomic association and prediction. The plant genome, 9(2):plantgenome2015–11.
- Tustison, N. J., Cook, P. A., Klein, A., Song, G., Das, S. R., Duda, J. T., Kandel, B. M., van Strien, N., Stone, J. R., Gee, J. C., et al. (2014). Large-scale evaluation of ants and freesurfer cortical thickness measurements. Neuroimage, 99:166–179.
- Urtio, V., Bhadra, S., and Rousu, J. (2019). Large-scale sparse kernel canonical correlation analysis. In International Conference on Machine Learning, pages 6383–6391. PMLR.
- Vounou, M., Nichols, T. E., Montana, G., Initiative, A. D. N., et al. (2010). Discovering genetic associations with high-dimensional neuroimaging phenotypes: A sparse reduced-rank regression approach. Neuroimage, 53(3):1147–1159.
- Wang, H., Nie, F., Huang, H., Kim, S., Nho, K., Risacher, S. L., Saykin, A. J., Shen, L., and Initiative, A. D. N. (2012). Identifying quantitative trait loci via group-sparse multitask regression and feature selection: an imaging genetics study of the adni cohort. Bioinformatics, 28(2):229–237.
- Wang, H., Nie, F., Huang, H., Risacher, S., Ding, C., Saykin, A. J., and Shen, L. (2011). Sparse multi-task regression and feature selection to identify brain imaging predictors for memory performance. In 2011 International Conference on Computer Vision, pages 557–562. IEEE.
- Wang, Y., Yan, G., Wang, X., Li, S., Peng, L., Tudorascu, D. L., and Zhang, T. (2023). A variational bayesian approach to identifying whole-brain directed networks with fmri data. The Annals of Applied Statistics, 17(1):518–538.
- Wang, Z., Novikov, A., Zolna, K., Merel, J. S., Springenberg, J. T., Reed, S. E., Shahriari, B., Siegel, N., Gulcehre, C., Heess, N., et al. (2020). Critic regularized regression. Advances in Neural Information Processing Systems, 33:7768–7778.
- Wehrle, F. M., Lustenberger, C., Buchmann, A., Latal, B., Hagmann, C. F., O’Gorman, R. L., and Huber, R. (2020). Multimodal assessment shows misalignment of structural and functional thalamocortical connectivity in children and adolescents born very preterm. Neuroimage, 215:116779.
- Wieling, M. and Nerbonne, J. (2009). Bipartite spectral graph partitioning to co-cluster varieties and sound correspondences in dialectology. In Proceedings of the 2009 Workshop on Graph-based Methods for Natural Language Processing (TextGraphs-4), pages 14–22.
- Wig, G. S., Laumann, T. O., and Petersen, S. E. (2014). An approach for parcellating human cortical areas using resting-state correlations. Neuroimage, 93:276–291.

- Witten, D. M., Tibshirani, R., and Hastie, T. (2009). A penalized matrix decomposition, with applications to sparse principal components and canonical correlation analysis. Biostatistics, 10(3):515–534.
- Woo, C.-W., Krishnan, A., and Wager, T. D. (2014). Cluster-extent based thresholding in fmri analyses: pitfalls and recommendations. Neuroimage, 91:412–419.
- Wu, Q., Zhang, Y., Huang, X., Ma, T., Hong, L. E., Kochunov, P., and Chen, S. (2021). A multivariate to multivariate approach for voxel-wise genome-wide association analysis. bioRxiv, pages 2021–11.
- Yohai, V. J. (2008). Optimal robust estimates using the kullback–leibler divergence. Statistics & probability letters, 78(13):1811–1816.
- Zalesky, A., Fornito, A., and Bullmore, E. T. (2010). Network-based statistic: identifying differences in brain networks. Neuroimage, 53(4):1197–1207.
- Zhang, A. and Xia, D. (2018). Tensor svd: Statistical and computational limits. IEEE Transactions on Information Theory, 64(11):7311–7338.
- Zhang, J., Sun, W. W., and Li, L. (2023). Generalized connectivity matrix response regression with applications in brain connectivity studies. Journal of Computational and Graphical Statistics, 32(1):252–262.
- Zhang, J., Wang, H., Zhao, Y., Guo, L., and Du, L. (2022). Identification of multimodal brain imaging association via a parameter decomposition based sparse multi-view canonical correlation analysis method. BMC bioinformatics, 23(3):1–14.
- Zhao, Z., Chen, C., Adhikari, B. M., Hong, L. E., Kochunov, P., and Chen, S. (2023). Mediation analysis for high-dimensional mediators and outcomes with an application to multimodal imaging data. Computational Statistics & Data Analysis, 185:107765.
- Zhou, H. and Li, L. (2014). Regularized matrix regression. Journal of the Royal Statistical Society. Series B, Statistical Methodology, 76(2):463.
- Zhu, H., Khondker, Z., Lu, Z., and Ibrahim, J. G. (2014). Bayesian generalized low rank regression models for neuroimaging phenotypes and genetic markers. Journal of the American Statistical Association, 109(507):977–990.
- Zhu, X., Suk, H.-I., Wang, L., Lee, S.-W., Shen, D., Initiative, A. D. N., et al. (2017). A novel relational regularization feature selection method for joint regression and classification in ad diagnosis. Medical image analysis, 38:205–214.
- Zhuang, X., Yang, Z., Curran, T., Byrd, R., Nandy, R., and Cordes, D. (2017). A family of locally constrained cca models for detecting activation patterns in fmri. NeuroImage, 149:63–84.